CHEMISTRY OF MATERIALS

ARTICLE

pubs.acs.org/cm

Structural and Photoluminescent Properties of Zn_2SiO_4:Mn^{2+} Nanoparticles Prepared by a Protected Annealing Process

Caroline Bertail,[†,‡] Sébastien Maron,[†] Valérie Buissette,[‡] Thierry Le Mercier,[‡] Thierry Gacoin,[*,†] and Jean-Pierre Boilot[†]

[†]Groupe de Chimie du Solide, Laboratoire de Physique de la Matière Condensée, CNRS UMR 7643, École Polytechnique, 91128, Palaiseau, France

[‡]Centre de Recherches d'Aubervilliers, Rhodia, 52, rue de la Haie Coq, 93308, Aubervilliers, France

Supporting Information

ABSTRACT: This works presents a new method for the production of colloidal suspensions of Zn_2SiO_4:Mn (ZSM) luminescent nanoparticles. The process consists in achieving a high temperature solid state reaction among silica nanoparticles homogenously dispersed within a ZnO matrix in large excess. Highly crystalline, well dispersed nanoparticles are recovered as a colloidal suspension after dissolution of the ZnO matrix in slightly acidic water. Yellow emitting β-Zn_2SiO_4:Mn or green emitting α- Zn_2SiO_4:Mn are obtained depending on the reaction temperature (either 800 or 900 °C) and the Mn content. $Zn_{2-2x}SiO_4$:Mn_x particles with x up to 3% can be obtained with a maximum relative emission efficiency of about 16% as compared to a bulk ZSM phosphor reference. The principle of this new synthetic route opens a new field of investigation for the production of colloidal dispersion of refractory compounds with a high crystallinity.

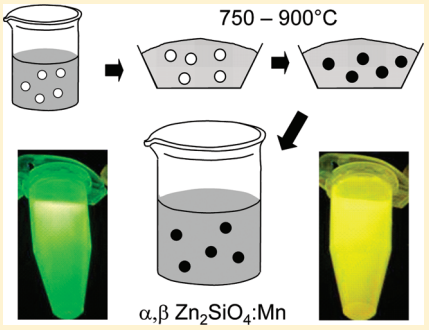

KEYWORDS: willemite, luminescence, green phosphor, nanomaterial, colloid, nanoparticles

INTRODUCTION

Willemite (Zn_2SiO_4) is a well-known host material for applications in the field of phosphors for light emitting devices.[1] Red, blue, and green colors may be obtained through doping with Eu^{3+}, Ce^{3+}, and Mn^{2+} ions, respectively.[2] Mn(II)-doped Zn_2SiO_4 green phosphor, often referred to as ZSM, is of particular interest because of its high luminescence efficiency, its high photostability (especially under VUV excitation), and the absence of moisture sensitivity. All this make it commonly used in fluorescent lamps, and in various display devices (field emission displays (FED), vacuum fluorescent displays (VFD), and plasma display panels (PDP)[3−5]).

As for many phosphor materials, synthesis of ZSM is usually achieved through conventional solid state reaction at high temperature.[4] The optimized product in term of chemical composition, oxidation state of the dopant, and crystallinity is commercially available for industrial applications. Improvement of the ZSM synthesis now concerns a better control of the grains' morphology and agglomeration state. These parameters are indeed poorly controlled in conventional solid state synthesis because the calcination temperatures required to have a perfect homogeneity of the chemical composition lead to the concomitant growth and agglomeration of the phosphor grains through sintering. Most studies rely on the intimate mixing of the precursors prior to their calcinations to decrease the required temperature of calcination. This can be achieved starting from molecular precursors or salts using spray pyrolysis,[6] sol−gel process,[7−9] mesoporous template routes,[10,11] solution combustion method,[12] or organometallic precursor routes.[13] All these methods lead to ZSM powders with submicrometric grain sizes.

The ultimate challenge for nanocrystalline materials synthesis is the elaboration of individualized particles with a controlled size. This would allow the further elaboration of materials with a perfectly controlled microstructure, and opens the way toward new original applications such as biological labels or transparent light emitting devices. Many examples such as YVO_4:Eu,[14] $LaPO_4$:Ce,Tb[16] or YAG:Ce[17] are now well-known for the elaboration of well dispersed oxide phosphor nanoparticles, most of them using colloid chemistry routes. Concerning ZSM, hydrothermal[18−20] and solvothermal[21−24] synthesis have been reported, leading to more or less dispersed nanoparticles.

Our group has been involved since many years on the elaboration of colloidal dispersions of phosphor materials, especially rare-earth doped $LaPO_4$ and YVO_4 obtained through simple reactions of precipitation in water.[14,15] As reported by many other groups on different phosphor compounds, investigation of the emission properties of the obtained particles usually show altered efficiencies as compared to related bulk reference. We recently reported that, in the case of YVO_4:Eu particles in the size range of about 30−40 nm, the main limitation of the emission does not arise from surface quenching but from defects in the volume of the particles or structural disorder resulting from the low temperature of synthesis.[14] This result was demonstrated

Received: February 25, 2011
Revised: April 16, 2011
Published: May 17, 2011

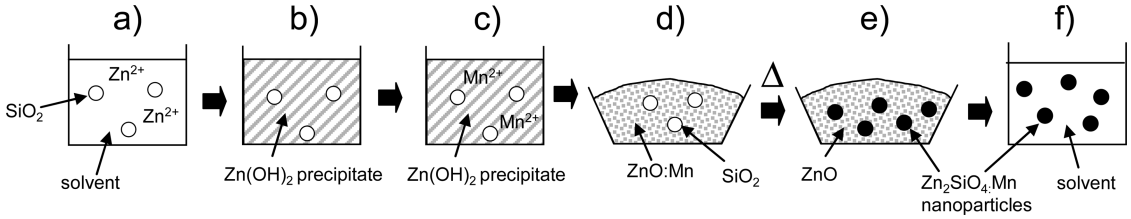

Figure 1. General scheme of the synthetic route investigated in this work. (a) Solution containing the zinc salt and silica particles, (b) precipitation of $Zn(OH)_2$ by addition of a base, (c) washing and addition of the Mn^{2+} salt, (d) drying and recovery as a powder, (e) calcination leading to the formation of the ZSM nanoparticles, and (f) selective dissolution of the ZnO matrix, washing, and recovery of the particles as a colloidal dispersion.

considering the drastic improvement of emission yield observed by achieving a so-called "protected annealing" treatment at 1000 °C.[25] This annealing process was achieved on particles dispersed in a silica matrix to prevent particles growth and sintering, and allowing their recovery as a colloidal suspension after dissolution of the matrix.

The main idea of the present work is to extend this strategy and develop a new synthetic procedure for the preparation of highly crystalline Zn_2SiO_4:Mn^{2+} colloidal nanoparticles obtained after a thermal treatment at high temperature. We focused our attention on the development of a process that relies on the in situ generation of nanoparticles within a ZnO matrix through solid state reaction between precursors at high temperature. The general process is shown on Figure 1.

The ZnO matrix aims to limit particles size and to preserve the nanoparticle dispersion during calcination. After its selective dissolution, non aggregated zinc silicate nanoparticles are expected to be recovered and dispersed in an appropriate solvent to get the colloidal suspension. ZnO was also chosen considering that it is a precursor of the ZSM phase and that it can be easily dissolved using slightly acidic water. Moreover, the ZnO/SiO_2 phase diagram only has ZSM as a definite compound so that stoichiometry in the presence of ZnO in large excess must be preserved. Small silica colloidal particles were used as precursor of the silicate component.

In this paper, we present our results on the investigation of the proposed strategy and on the effect of several parameters among which are the temperature of calcination and the Mn content. The obtained particles are fully characterized in terms of size, crystalline structure, and dispersion state. We show that the temperature of calcination allows governing not only the size of the particles but also their crystalline phase leading to particles with either green or yellow emission properties. All these results are discussed in relation with a mechanism for the particles formation corresponding to the initial strategy that was proposed.

EXPERIMENTAL SECTION

Synthesis of Zn_2SiO_4:Mn^{2+} colloidal nanoparticles was achieved following the process schematically described on Figure 1.

Mixture of Precursors to the Solid State (Steps a to d of Figure 1). A 0.896 mol·L^{-1} solution of $Zn(OAc)_2.2H_2O$ (98+% ACS, Aldrich) in dimethylformamide (DMF, 99.9+%, Aldrich) (10 mL, 8.96 mmol) was mixed with 83 μL of a colloidal silica sol (NISSAN MAST, pH = 2, diameter =15 nm, S = 263 m^2/g, [SiO2] = 323 g/L in methanol) under magnetic stirring. The clear and colorless resulting mixture was subsequently slowly added into a basic aqueous solution of tetramethylammonium hydroxide (25 wt % in water, Sigma Aldrich) (25 mL, 0.5 mol·L^{-1}) under vigorous stirring, leading to a white precipitate. The pH at the end of the addition is about 7.3. The precipitate was homogenized by sonication and washed with distilled water by centrifugation (11363 g − 1 h). The white precipitate was then dispersed in 150 mL of an aqueous solution of $MnCl_2 \cdot 4H_2O$ (98+% ACS, Aldrich) and homogenized by sonification. A white powder was finally obtained by evaporation of water under mild conditions (40 °C, 30 Torr).

Thermal Treatment for Solid State Reaction (Step d of Figure 1). The powder was put into a tubular furnace and heated between 810 and 915 °C for 4 h under argon atmosphere.

Matrix Dissolution and ZSM Colloidal Suspension Recovery (Step e of Figure 2). The calcined powder, a mixture of ZnO and Zn_2SiO_4, was washed with a 5 mol·L^{-1} solution of acetic acid (glacial, Carlo Erba) in dimethylformamide containing 5% vol H_2O. The amount of acetic acid used was taken as 12 mol equiv as compared to ZnO. After 10 min under stirring at 60 °C, the suspension was sonicated for 2 min and centrifuged (11363 g − 1 h). The precipitate was then purified by washing twice with DMF. The whole process is repeated a second time. At the end of this step, the ZnO matrix had been dissolved and zinc silicate particles were recovered as a suspension in dimethylformamide.

Finally, ZSM nanoparticles were transferred into ethyleneglycol (99.8+%, Aldrich) by centrifugation/dispersion using sonication. A few droplets of an aqueous sodium poly(acrylic acid) solution (M_w = 1200, 45 wt % in water, Aldrich) were then added, and the pH was adjusted to 9 with an aqueous solution of tetramethylammonium hydroxide (1 mol·L^{-1}).

Characterizations. X-ray diffraction (XRD) studies were performed on nanocrystals powders using a Philip X-Pert diffractometer with Cu Kα radiation (λ = 1.54 Å). Dynamic light scattering experiments were carried out with Zetasizer NanoZS equipment supplied by Malvern. The synthesized products were characterized using a Hitachi FEG S4800 scanning electron microscope (SEM) and a Philips CM 30 transmission electron microscope (TEM) operating at 300 kV. The samples for TEM were prepared by first depositing a droplet of polymer (polyethyleneimine) and then a droplet of colloidal solution onto a TEM grid. A Netzsch thermoanalyzer STA409 was used for simultaneous thermal analysis combining thermogravimetry (TG) and differential thermal analysis (DTA) with a heating rate of 10 °C min^{-1} in argon. ^{29}Si MAS NMR characterizations of powders were achieved on a TecMag Apollo spectrometer with a 8.46 T wide-bore Oxford magnet. The MAS experiments were performed with a Brüker probe equipped with 4 mm ZrO2 rotors at a spinning rate of 14 kHz. The ^{29}Si MAS experiments were run with a recycle time of 500 s, 90° pulse lengths (2.3 ms), a dwell time at 20 μs, a dead time at 25 μs, and 680 scans in each experiment. The ^{29}Si chemical shifts were referenced to tetraethoxysilane (δ(Si) = −82 ppm). All NMR experiments were conducted with non doped zinc silicate to avoid the effects of paramagnetic ion. Luminescence spectra and lifetime measurements were recorded on a Hitachi F-4500 spectrofluorometer. Relative quantum yields were determined by comparing the integrated emission of as-synthesized zinc silicate nanoparticles with the emission under the same excitation wavelength of a micrometer sized zinc silicate obtained by solid state reaction without ZnO in excess.

dx.doi.org/10.1021/cm2005902 |Chem. Mater. 2011, 23, 2961–2967

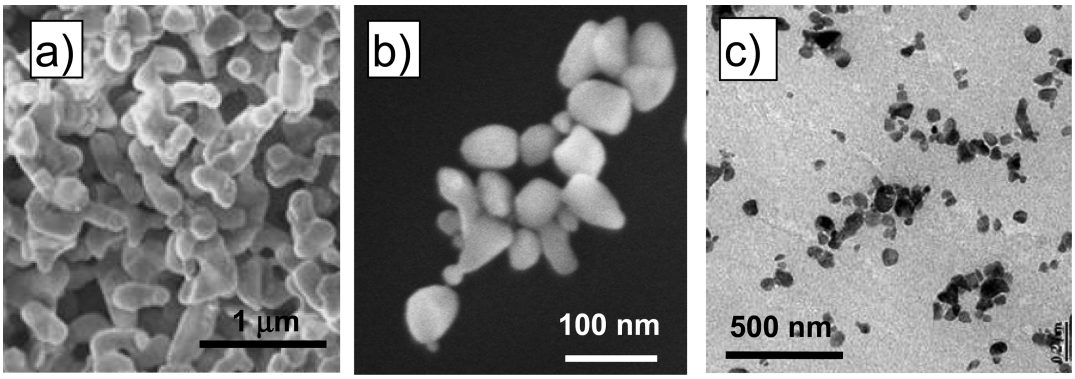

Figure 2. SEM image of ZSM colloidal particles obtained in the absence (a) or in the presence (b) of the ZnO matrix evidencing its efficiency to limit the size and the sintering of the particles. TEM image of the same particles as in b (c).

Zinc and manganese atomic contents in nanoparticles were deduced from chemical analysis performed by inductively coupled plasma emission spectrometry (ICP-ES) after dissolution of nanoparticles in acidic solution.

RESULTS AND DISCUSSION

Process. Preliminary experiments were achieved to determine the best precursors to be chosen to follow the proposed synthesis protocol. To avoid the presence of residual elements that could interfere with the ZSM phase formation, alkaline counterions were prohibited. Zinc acetate was chosen since the acetate would be removed during calcination, and neutral colloidal silica instead of silicates. A critical step of the process is to achieve the appropriate homogeneous dispersion of the silica particles within the ZnO host matrix, that is, to avoid their segregation leading to uncontrolled dispersion and growth of the obtained ZSM particles. This is all the more difficult considering the high ionic strength of the solution resulting from the presence of zinc salt at high concentration. We found that using DMF as the solvent and colloidal silica in methanol allows to mix Zn and Si precursors without any precipitation, thus preserving their intimate mixing. Starting from this homogeneous dispersion, precipitation of the $Zn(OH)_2$ matrix was then achieved by slow addition of tetramethylammonium hydroxyde. Complete precipitation of the ions was monitored by controlling the pH increase up to about 7. At this step, Mn^{2+} ions are added after a rough washing of the precipitate to remove part of the counterions. Note that Mn was added in a second step and not mixed initially with the Zn ions because of the addition of a strong base that leads to precipitation of Mn oxo/hydroxide (seen through the appearance of a brown color). The neutral pH at the time of Mn addition to the precipitate allows preserving the 2+ oxidation state.

After drying of the precipitate, the recovered powder contains the silica particles and the Mn ions dispersed within the ZnO matrix. Solid state reaction is then achieved by high temperature treatment under argon to avoid Mn oxidation. The formation of the ZSM phase (which is the only compound that can be obtained as referring from the ZnO/SiO_2 phase diagram) was found to start at about 750 °C as checked by X-ray diffraction (Figure 2).

The next step was the recovery of the particles as a colloidal solution through dissolution of the ZnO matrix under acidic conditions. Preliminary studies have shown that the ZSM particles may dissolve in acidic aqueous solution. The problem was circumvented by achieving the dissolution using acetic acid in DMF with 5% water (this water was found necessary to allow the dissolution of the formed Zn salt). The total reaction yield was found to be 45−50% for 810 °C (but residual SiO_2 was detected in the solid) and 60−65% at 915 °C.

Zêta potential measurements were achieved to study the redispersion of the particles obtained after the ZnO dissolution step (see Supporting Information). Over the full range of pH, the surface charge of zinc silicate particles was found to be negative, with a value lower than −30 mV (assumed to be required to ensure correct dispersion) for pH between 10 and 12. Nevertheless, dispersion under these conditions of pH did not give satisfactory results, presumably because of surface reactivity of silanols or dissolution/precipitation problems. Particles were preferably dispersed into ethyleneglycol, which is known to be a good dispersing solvent for oxides while being more chemically neutral than water. This solvent was also chosen regarding the further studies on luminescence that requires a non absorbing solvent under UV excitation. Slight improvement of the colloid dispersion was also observed by adding poly(acrylic acid) , leading to a zêta potential of −55 mV.

Characterization of the colloids by dynamic light scattering experiments leads to a typical size of about 180 nm in term of volumic fraction analysis (see Supporting Information). Electron microscopy images are shown on Figure 2. Well individualized particles are observed, evidencing the role of the ZnO matrix when comparing with the image of a stoichiometric sample obtained without ZnO in excess (Figure 2a). The size of the particles are typically of 40−70 nm for particles heated at 810 °C and of 80−100 nm for particles heated at 915 °C. This is compatible with the coherence length as measured from X-ray diffraction, attesting to the good crystallinity of the particles.

Structural Characterization of the Particles. Willemite Zn_2SiO_4 is a natural orthosilicate with a phenacite like structure (space group $R\bar{3}$). In this structure, Zn^{2+} ions occupy two different sites both having four oxygen atoms as their nearest neighbors in a slightly distorted tetrahedral (T_d) configuration. In a previous work, electron paramagnetic resonance (EPR) studies showed that Mn could be incorporated on both Zn sites,[26] since the two ions have identical valency and very close ionic radii (0.60 Å for Zn^{2+} and 0.66 Å for Mn^{2+} (CN = 4)[27]). Two polymorphs of the α-Zn_2SiO_4 phase (the only stable form) exist and show different luminescent properties: the β-form, exhibiting a yellow luminescence, and the γ-form, with a red luminescence.[28−30] β-Zn_2SiO_4 has been observed in the case of

dx.doi.org/10.1021/cm2005902 |Chem. Mater. 2011, 23, 2961–2967

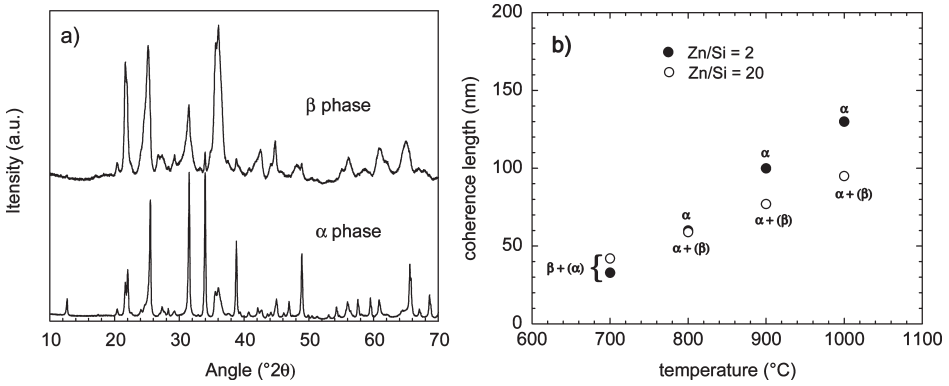

Figure 3. (a) X-ray patterns of zinc silicate nanoparticles: nanoparticles heated at 785 °C with the β-Zn_2SiO_4 monoclinic structure (JCPDS 19-1479) and Nanoparticles heated at 915 °C with the α-Zn_2SiO_4 phenacite structure (JCPDS 37-1485). (b) Evolution of coherence length as a function of the temperature of calcination with (ratio Zn/Si = 20, empty dots) or without matrix (ratio Zn/Si = 2, plain dots).

very small grain size, obtained after rapid cooling of SiO_2/ZnO mixtures thermally treated at high temperature (about 1500 °C).[29] It was also obtained from the thermal dehydration of hemimorphite ($Zn_4Si_2O_7(OH)_2H_2O$)[30] or through confined reaction within a porous host media.[10]

β-Zn_2SiO_4 is thermodynamically metastable and converts into the stable α-phase upon prolonged heating. The phase transition is analogous to ordinary topotactic changes. The oxygen framework tends to remain largely unchanged, and smaller highly charged cations (Si and Zn in our case) tend to migrate most readily.[31] The structure of β-Zn_2SiO_4 is not fully characterized. It probably derives from a distorted tridymite- or cristobalite-like framework in which half of the silicon is replaced by zinc and additional atoms of zinc introduced into suitable interstices (in 6-fold coordination).

Figure 3 shows the powder diffraction patterns of zinc silicate nanoparticles obtained after 4 h at 785 and 915 °C respectively. Diagram from the sample heated at 785 °C is found to correspond to the β-Zn_2SiO_4 structure. Some contribution in the baseline from an amorphous phase, probably SiO_2, indicates that the reaction is not complete under these conditions. Concerning the sample heated at 915 °C, it is found to correspond to α-Zn_2SiO_4, with still some residue of β-Zn_2SiO_4 that are not found when the reaction is achieved under stoichiometric condition (Zn/Si = 2, i.e., without a ZnO matrix).

Evolution of the coherence length as a function of the temperature of annealing was determined using the Sherrer law on the (113) peak of the α phase or the (−132) peak of the β phase respectively. Results are shown on Figure 3b on a sample with Zn/Si equal to 20 (large excess of ZnO) and 2 (stoichiometric) for comparison. At 800 °C, for which a significant part of the precursors has reacted, the coherence length is already about 60 nm and no clear differences are seen depending on the excess of ZnO. We conclude that very small particles are not obtained for a significant conversion rate of the precursor. Increasing the temperature up to 1000 °C leads to an increase of the coherence length in both cases, but the sample with ZnO in large excess exhibits a much lower domain size. In the ideal case, a saturation of the coherence length would have been expected if the solid-state reaction was just confined at the ZnO/SiO_2 interface. The fact that a continuous increase is observed may be explained either by some aggregation of the initial SiO_2 particles or by some significant diffusion of the silicate within the ZnO matrix (probably through its porosity in this case) at the temperature required to complete the formation of the ZSM phase. Further conclusion would probably require a detailed characterization of the SiO_2 dispersion within the ZnO matrix prior to calcination, for example, using electron microscopy.

The interesting point is nevertheless that we are able, by playing with temperature, to synthesize particles exhibiting either the β-phase (around 800 °C) or the α-phase (around 900 °C). The coherence lengths were found to be about 30 to 40 nm for β-phase and 80 nm in size for α-phase, respectively. This is consistent with particle sizes observed on SEM pictures (Figure 2), indicating that the particles are mainly monocrystalline.

A first explanation why the β-phase is obtained at low temperature while the α-phase is obtained at higher temperature could be that the mechanism of phase formation is kinetically in favor of the metastable β-phase, which further converts into α-phase upon increasing temperature. This is consistent with TGA/TDA measurements performed on nanoparticles powders (Supporting Information) that exhibit an exothermic signal near 900 °C which corresponds to the transformation of β-willemite into the α-phase.[7] But another possible explanation is that particles exhibit the β-phase because of their small size and a lower surface energy of this phase as compared to the α-phase, the latter having a lower volume energy. In that case, the β- to α- transformation upon increasing from 700 to 900 °C would be explained just by an increase of particle size and thus a decrease of the predominance of surface versus volume energies. The limited efficiency of the ZnO matrix to limit particle growth upon heating does not allow a definitive conclusion. Nevertheless, the presence of a small amount of β-phase, even in samples heated at 1000 °C, plays in favor of the second explanation (lower surface energy of the β-phase). Such a size dependent crystalline structure has been commonly observed in many other systems (for example CdS[32]).

Starting from our ability to prepare particles with the two different structures, samples were characterized using solid state ^{29}Si-MAS NMR spectroscopy to study the environment and the connectivity of SiO_4^{4-} structural units and thus tentatively explain the difference of emission properties between the two structures. Figure 4 displays the spectra of almost pure β-Zn_2SiO_4 and α-Zn_2SiO_4 samples obtained at 785 and 915 °C respectively, and one sample obtained under intermediate conditions (850 °C) displaying a mixture of both the α and the β-phases.

In these experiments, all spectra exhibit a sharp peak located at −65 ppm and −71 ppm for the α and β-phases, respectively.

dx.doi.org/10.1021/cm2005902 |*Chem. Mater.* 2011, 23, 2961–2967

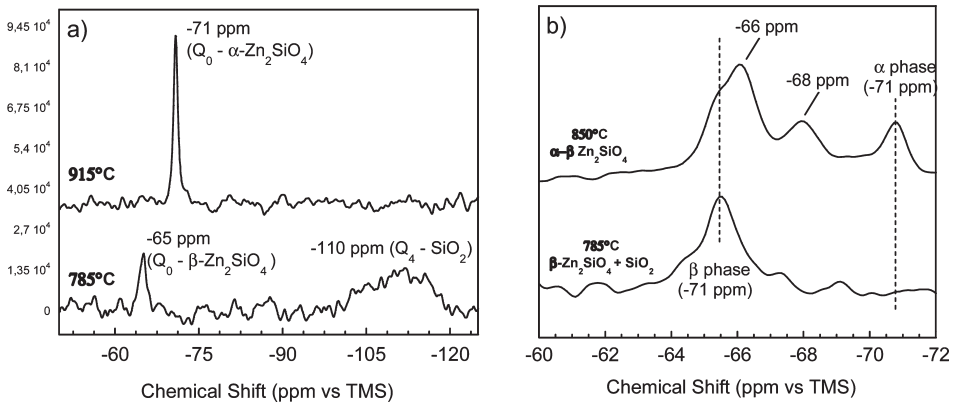

Figure 4. ^{29}Si MAS NMR spectra. (a) β-Zn_2SiO_4 and α-Zn_2SiO_4 sample obtained at 915 and 785 °C, respectively. (b) Spectra of a sample obtained at an intermediate temperature (850 °C) exhibiting additional contributions as compared to the β phase sample .

These peaks are characteristic of monomeric Q_0 orthosilicate units as expected from the structures (Q_n represents SiO_4 units that share their bonds with n other neighboring silicon atoms).[13,33] In the case of the β-sample, a contribution is clearly detected at −110 ppm, corresponding to Q_4 groups from amorphous SiO_2 resulting from the incomplete reaction. The sharpness of the Q_0 peaks in both samples indicates that the silicon atoms have a precise crystallographic environment, corresponding to the crystalline phase as detected by X-ray diffraction. The 6 ppm difference between the Q_0 signals from the two structures suggests a stronger electronic density on the silicon in the β phase.[34]

Figure 4b displays the spectra in the −62 to −72 ppm range of a sample obtained at an intermediate temperature (850 °C), and exhibiting a mixture of α- and β-phases as observed in the X-ray diagrams. The NMR spectra indeed shows the peaks at −65 ppm and −71 ppm which are characteristic of the β-phase and α-phase, respectively, but at least two other peaks at intermediate values of chemical shift (−66 and −68 ppm) are also clearly observed. It thus seems that this sample not only contains a mixture of α and β-phase domains, but also intermediate phases that could correspond to intermediate environments, resulting from the progressive topotactic transition between the two phases. We note that such a progressive transition, involving stacking faults and twin boundaries has also been observed in II−VI semiconductors' nanocrystals[32]

Mn^{2+}-Incorporation into the Nanoparticles. In our synthetic process, the Mn^{2+} ions are added in the ZnO matrix which is in large excess. The question is then to determine its degree of incorporation inside the ZSM particles, that is, the final distribution of manganese between the ZnO matrix and the particles. For this study, different amounts of Mn salt have been added in the initial formulation, varying between 0.1 and 1% in term of $Mn/(Mn + Zn_{total})$ molar ratio. The final amount of Mn within the particles was determined by ICP elemental analysis (Supporting Information). Whatever the initial amount of Mn and the temperature of synthesis between 810 and 915 °C leading to the α and β-phase, respectively, the concentration of Mn in the particles is found to be about 3 times higher than in the initial ZnO composition. This shows that the Mn ions have a somewhat higher affinity for the silicate structure than for ZnO.

For Mn concentration (in term of Mn/[Mn + Zn] molar ratio) of more than 3 mol % in the particles, particles were found to exhibit a brown color. X-ray diffraction analysis of the

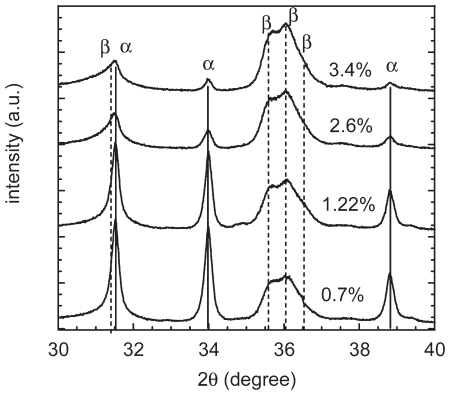

Figure 5. Evolution of X-ray diffraction patterns of four samples containing an increasing Mn rate.

corresponding sample shows that this color appears concomitantly with a new phase that coexists with the ZSM and was indentified as $ZnMn_2O_4$ phase (JCPDS 24-1133; Supporting Information)). 3 mol % thus appears to be the maximum Mn content that can be incorporated inside the ZSM phase through this process.

Another effect of Mn incoproration inside the particles is that it was found to influence the β-phase stability. Figure 5 displays XRD patterns of samples prepared at 915 °C with increasing $Mn/(Zn + Mn)$ molar ratio from 0.7% to 3.4%.

It appears clearly that the β-phase fraction increases with Mn content. A first explanation would be that the Mn ions decrease the size of the particles, for example, acting as nucleation centers, but no clear evolution of coherence length and particle size could be seen. Another explanation is that for a given particle size, the Mn ions help in stabilizing the β-structure. It is all the more possible that, in the β-structure, half the Zn are in tetrahedral sites and half in octahedral sites, while in the α-phase all are in tetrahedral sites. As octahedral coordinance fits better to the Mn^{2+} ionic radius, this could explain the stabilizing effect of the Mn for the β-phase.

Emission Properties of the Particles. Figure 6 displays the emission from colloidal dispersions of particles with the α- and β-phases respectively. A clear difference of emission is observed from yellow (β-) to green (α-) color,[24] all the more pronounced because the eye spectral sensitivity is very high.

In both cases, the radiative emission is attributed to the $^4T_1$-$^6A_1$ spin flip transition within the d-electrons of the Mn^{2+} ion.[3] This transition is forbidden in nature so that the emission

dx.doi.org/10.1021/cm2005902 |Chem. Mater. 2011, 23, 2961–2967

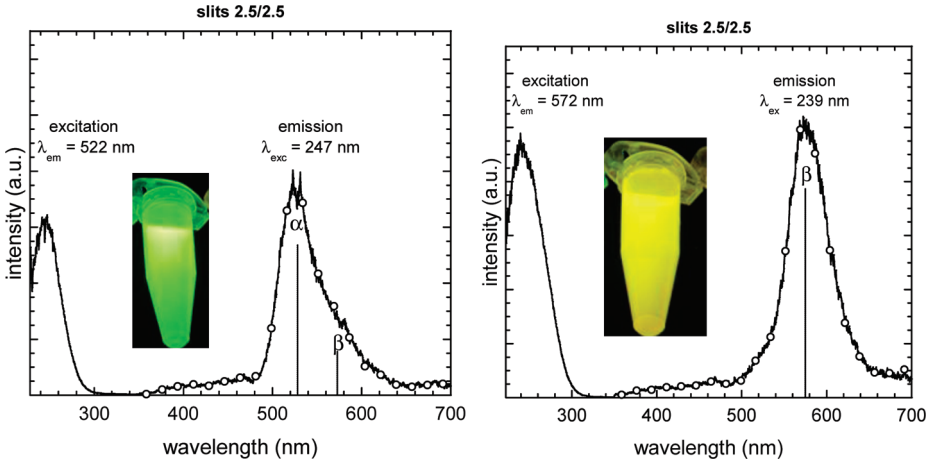

Figure 6. Excitation and emission spectra of α-Zn_2SiO_4 (left) and β-Zn_2SiO_4 (right) colloidal suspensions. Inset: emission of the samples as observed by the eyes under 254 nm UV illumination.

lifetime is very long (decay time at 10% ($\tau_{10\%}$) around 30 ms).[4] Excitation of the emitting $^4T_1$ level occurs after absorption of UV light by the Mn^{2+} in its ground states, leading to its oxidation into Mn^{3+} and the promotion of the electron into the conduction band of the host silicate. The electron in the conduction band then relax to the $^4T_1$ excited state through non radiative processes, and the $^4T_1$ to $^6A_1$ radiative transition follows leading to green emission peaking at 525 nm for the α-phase and yellow luminescence peaking at 570 nm for the β-phase.[4,10,24] Lifetime measurements (not shown) give values of 22 ms for the α-phase (0.7% Mn doping) and 35 ms for the β-phase (3.4% Mn doping).[4,10]

The origin of the difference of spectroscopic properties between the two phases has to be found in the difference of Mn crystal site within the host Zn_2SiO_4 matrix. The variation of energy of the $^4T_1$ and $^6A_1$ levels as a function of the crystal field in a tetrahedral or octahedral environment is given by the corresponding Tanabe−Sugano diagram [3, Supporting Information]. Considering the green and yellow emission of the α and β phases, respectively, one thus expects a stronger ligand field around the Mn^{2+} ion in the β-phase. In the α-phase, all possible sites for the Mn (i.e., Zn sites) are tetrahedral, whereas in the β-phase half are octahedral and half are tetrahedral. A first possibility to explain a higher ligand field in the β phase could be that the Mn ions are still in the tetrahedral sites, but the difference of structure leads to a higher crystal field. Nevertheless, this seems not to be consistent with the chemical shift variation between the two phases as observed in ^{29}Si NMR. It was indeed concluded that the β-phase exhibits a higher electron density on the silicon atom, which would then lead to a lower ligand field for neighboring Zn or Mn ions. It thus appears as more probable that the difference of ligand fields, and resulting spectroscopic properties, originates from a difference of location of the Mn ions: in tetrahedral sites for the α phase and octahedral for the β phase. A better characterization of the β-phase would be required to confirm this assumption, but we note that this is in accordance with the discussion on the effect of stabilization of the β-phase by the Mn ions, explained by a better fit of the Mn^{2+} ionic radius to octahedral sites.

The Mn^{2+}activator concentration is well-known to play an important role for the optimization of light emission efficiency in phosphors. The influence of Mn content on photoluminescence intensity has been investigated on powders synthesized at 915 °C by relative emission yield measurements with reference to a bulk ZSM material. Results are presented on Figure 7.

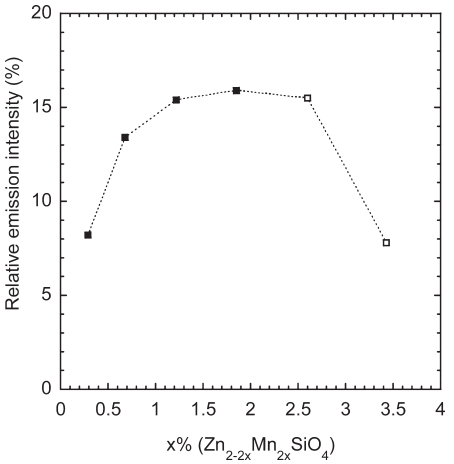

Figure 7. Relative quantum yield as a function of Mn content as measured on powders of nanoparticles synthesized at 915 °C with reference to a micronic ZSM powder. White squares correspond to samples with a brownish color because of the presence of the $ZnMn_2O_4$ phase.

Concerning bulk ZSM, the maximum emission yield is of 70−80% for an optimum Mn content of about 5−8%.[4,24] Higher amounts lead to a decrease of the emission properties as a result of Mn−Mn interactions. In the case of our particles, maximum emission intensity is found to be 16% as compared to a bulk reference. This value is reached for Mn content of about 2%, which is thus lower than the optimal content for the bulk materials. The difference of emission yield should be first explained by the limited efficiency of Mn incorporation in our nanoparticles. Nevertheless, reported value of emission yield versus Mn content show that the emission yield of the bulk compound doped with 2% Mn is already about 80% of the maximum, which means the improvement between 2% and 5−8% is not so important.[4] We must then conclude that some alteration of the emission may still be related to surface and residual defects within the particles. Refering to our previous work,[14] we could nevertheless expect these effects to be of less

importance considering the high temperature of synthesis of the particles (nearly the same as the bulk material) and their relatively big size (>50 nm) so that surface effects are expected to be limited. We then note that dielectric effects should also be discussed similarly to what has been evidenced in the case of YVO4:Eu particles.[14] In this case, decrease of emission yield (from 70% to 40%) was shown to result from an increase of radiative lifetime in nanoparticles because of a lower effective dielectric constant nearby the particles ($n_{ZSM} = 2.1$[35]). Such an effect was also shown to be all the more important that the radiative lifetime of the bulk emission is high and if there is a competition with residual non radioactive processes (i.e., deviation from 100% quantum yield). This is clearly the case for the ZSM bulk compound which exhibits a very high radiative lifetime (several tens of milliseconds) and a quantum yield of 70−80%. This explanation should nevertheless be discussed on the basis of a more detailed spectroscopic analysis.

CONCLUSION

The aim of this work was to investigate a process allowing the elaboration of dispersed colloidal particles of Zn_2SiO_4:Mn with a controlled size, obtained after a high temperature treatment of calcination (700 °C−1000 °C). The objective was to recover dispersible particles with an excellent crystallinity, thus exhibiting improved emission properties as compared to particles obtained through usual colloid chemistry techniques at low temperature. The process that was investigated consists in (i) intimate mixing of silica particles within a ZnO matrix in large excess, (ii) thermal treatment at high temperature (700−900 °C) of the obtained composite powder, and (iii) recovery of the Zn_2SiO_4:Mn particles dispersion through dissolution of the ZnO host matrix. Characterization of the obtained particles evidenced the role of the ZnO matrix to limit the aggregation and growth of the Zn_2SiO_4:Mn particles, thus providing a proof of concept of this protected calcination strategy. The size and the crystal structure of the particles were found to depend on the temperatures of calcination: yellow emitting β-Zn_2SiO_4:Mn particles with a diameter of 40−70 nm are obtained at about 800 °C, while green emitting α-Zn_2SiO_4:Mn particles with a diameter of 80−100 nm are obtained at about 900 °C. The size induced phase transition is discussed in term of surface/volume energy of the two phases. The Mn insertion was characterized, showing that a maximum of about 2% could be obtained before the formation of a parasitic $ZnMn_2O_4$ phase. The Mn^{2+} insertion was shown to stabilize the β-phase, which is explained by a better fit of the Mn ions inside the octahedral sites that are present only in this structure. Finally, the emission yield of the particles was measured to be 16% as compared to a bulk reference. This value, quite high for oxide nanoparticles in solution, is expected to be limited not only by residual defects but also by dielectric effects as previously shown in highly crystalline YVO_4:Eu particles.[14] The latter point will be the subject of further investigations.

ASSOCIATED CONTENT

Supporting Information. Additional information as noted in the text. This material is available free of charge via the Internet at http://pubs.acs.org.

AUTHOR INFORMATION

Corresponding Author

*E-mail: thierry.gacoin@polytechnique.fr. Phone: 33 (1) 69 33 46 56.

ACKNOWLEDGMENT

This work was partly funded by Rhodia, CNRS and Ecole Polytechnique.

REFERENCES

(1) Shionoya, S., Yen, W.M., Eds.; *Phosphor Handbook*; CRC Press: Boca Raton, FL, 1999.
(2) Zhang, Q. Y.; Pita, K.; Kam, C. H. *J. Phys. Chem. Solids* **2003**, *64*, 333–338.
(3) Blasse, G. Grabmaier, B. C. *Luminescent Materials*; Springer Verlag: New York, 1994.
(4) Morell, A.; Elkhiati, N. *J. Electrochem. Soc.* **1993**, *140*, 2019.
(5) Van der Kolk, E.; Dorenbos, P.; Van Eijk, C. W. E.; Bechtel, H.; Justel, T.; Nikol, H.; Ronda, C. R.; Wiechert, D. U. *J. Lumin.* **2000**, *87−89*, 1246–1249.
(6) Kang, Y. C.; Park, S. B. *Mater. Res. Bull.* **2000**, *35*, 1143–1151.
(7) Lin, C. C.; Shen, P. *J. Non-Cryst. Solids* **1994**, *171*, 281–289.
(8) Copeland, T. S.; Lee, B. I.; Qi, J.; Elrod, A. K. *J. Lumin.* **2002**, *97*, 168–173.
(9) Kwon, M. S.; Kim, C. J.; Park, H. L.; Kim, T. W.; Lee, H. S. *J. Mater. Sci.* **2005**, *40*, 4089–4091.
(10) Taghavinia, N.; Lerondel, G.; Makino, H.; Yamamoto, A.; Yao, T.; Kawazoe, Y.; Goto, T. *J. Cryst. Growth* **2002**, *237−239*, 869–873.
(11) Li, B.; Zhou, J.; Zong, R. L.; Li, L. T. *High Perform. Ceram. III* **2005**, *280−283*, 541–544.
(12) Sreekanth Chakradhar, R. P.; Nagabhushana, B. M.; Chandrappa, G. T.; Ramesh, K. P.; Rao, J. L. *J. Chem. Phys.* **2004**, *121*, 10250–10259.
(13) Roy, A.; Polarz, S.; Rabe, S.; Rellinghaus, B.; Zahres, H.; Kruis, F. E.; Driess, M. *Chem.—Eur. J.* **2004**, *10*, 1565–1575.
(14) Mialon, G.; Türkcan, S.; Alexandrou, A.; Gacoin, T.; Boilot, J.-P. *J. Phys. Chem. C* **2009**, *113*, 18699–18706.
(15) Buissette, V.; Giaume, D.; Gacoin, T.; Boilot, J.-P. *J. Mater. Chem.* **2006**, *16*, 529–539.
(16) Haase, M.; Riwotzki, K.; Meyssamy, H.; Kornowski, A. *J. Alloys Compd.* **2000**, *303−304*, 191–19.
(17) Kasuya, R.; Kawano, A.; Isobe, T.; Kuma, H.; Katano *J. Appl. Phys. Lett.* **2007**, *91*, 111916.
(18) Li, Q. H.; Komarneni, S.; Roy, R. *J. Mater. Sci.* **1995**, *30*, 2358–2363.
(19) Wan, J. X.; Wang, Z. H.; Chen, X. Y.; Mu, L.; Yu, W. C.; Qian, Y. T. *J. Lumin.* **2006**, *121*, 32–38.
(20) Ahmadi, T. S.; Haase, M.; Weller, H. *Mater. Res. Bull.* **2000**, *35*, 1869–1879.
(21) Lou, T. J.; Zeng, J. H.; Lou, X. D.; Fu, H. L.; Wang, Y. F.; Ma, R. L.; Tong, L. J.; Chen, Y. L. *J. Colloid Interface Sci.* **2007**, *314*, 510–513.
(22) Miki, T.; Ogawa, T.; Isobe, T.; Sfihi, H. *J. Sol-Gel Sci. Technol.* **2004**, *31*, 73–77.
(23) An, J.-S.; Noh, J. H.; Cho, I.-S.; Roh, H.-S.; Kim, J. Y.; Han, S. H.; Hong, K. S. *J. Phys. Chem. C* **2010**, *114*, 10330–10335.
(24) Mai, M.; Feldmann, C. *Solid State Sci.* **2009**, *11*, 528.
(25) Mialon, G.; Gohin, M.; Gacoin, T.; Boilot, J. P. *ACS Nano* **2008**, *2*, 2505–2512.
(26) Klaska, K. H.; Eck, J. C.; Pohl, D. *Acta Crystallogr., Sect. B* **1978**, *34*, 3324–3325.
(27) Shannon, R. *Acta Crystallogr., Sect. A* **1976**, *32* (5), 751–767.
(28) Schleede, A.; Grühl, A. *Z. Elektrochem.* **1923**, *29*, 411–412.
(29) Rooksby, H.; McKeag, A. *Trans. Faraday Soc.* **1941**, *37*, 308–311.
(30) Taylor, H. F. W. *Am. Mineral.* **1962**, *47* (7−8), 932–944.
(31) Williamson, J.; Glasser, F. *Phys. Chem. Glasses* **1964**, *5* (2), 52–59.
(32) Ricolleau, C.; Audinet, L.; Gandais, M.; Gacoin, T. *Eur. Phys. J. D* **1999**, *9*, 1–6.
(33) Cannas, C.; Casu, M.; Lai, A.; Musinu, A.; Piccaluga, G. *J. Mater. Chem.* **1999**, *9*, 1765–1769.
(34) Engelhardt, G.; Michel, D. *High-Resolution Solid-State NMR of Silicates and Zeolites*; John Wiley & Sons: Chichester, 1987.
(35) Li, B.; Zhou, J.; Zong, R.; Fu, M.; Li, L.; Li, Q. *J. Am. Ceram. Soc.* **2006**, *89*, 2308–2310.